Ray-tracing code TRAVIS for ECR heating, EC current drive and ECE diagnostic

N. B. Marushchenko, Y. Turkin, H. Maassberg

Max Planck Institute for Plasma Physics, EURATOM Association, Wendelsteinstr. 1, D-17491 Greifswald, Germany

Abstract

A description of the recently developed ray-tracing code `TRAVIS` is given together with the theoretical background, results of benchmarking and examples of application. The code is written for electron cyclotron studies with emphasis on heating, current drive and ECE diagnostic. The code works with an arbitrary 3D magnetic equilibrium being applicable for both stellarators and tokamaks. The equations for ray tracing are taken in the weakly relativistic approach, i.e. with thermal effects taken into account, while the absorption, current drive and emissivity are calculated in the fully relativistic approach. For the calculation of ECCD, an adjoint technique with parallel momentum conservation is applied. The code is controlled through a specially designed graphical user interface, which allows the preparation of the input parameters and viewing the results in convenient (2D and 3D) form.

Keywords: electron cyclotron resonance heating, current drive, ECE diagnostic, ray tracing

1. Introduction

Propagation of radio-frequency (RF) waves in slightly inhomogeneous plasmas can be described well within the WKB approximation, also called the geometrical optics (GO) approach (see, e.g. Refs. [1–3]). If $c/\omega \ll L$ with ω the wave frequency and L the inhomogeneity scale, the RF beam can be discretized by independent rays each following its own trajectory. This ray-tracing technique is a tool for simulating electron cyclotron resonance heating (ECRH), current drive (CD), and electron cyclotron emission (ECE) diagnostics in high temperature plasmas [4]. However, this approach fails near focal points where the width of the RF beam, d, becomes comparable with the wave length. Beam-tracing techniques, complex eikonal and quasi-optic approaches [5–9], below all referred as beam-tracing, include higher order effects and are necessary for scenarios with highly focused beams, where $d \lesssim \sqrt{cL/\omega}$ and such effects as diffraction and aberration become significant. In the more typical case, when the RF beam is not perfectly focused or even diverges, the ray-tracing technique is well applicable and even preferable, especially if the width of divergent beam is comparable to the characteristic scale of the plasma (in this case, the beam-tracing technique based on the paraxial approach fails).

A common approach, exploited in the ray- and beam-tracing codes (see, e.g. Refs. [8, 10, 11]), is the assumption that the ray trajectory can be described with sufficient accuracy by the "cold" dispersion relation taken as Hamiltonian. However, near the cyclotron resonance, the ray

trajectories can be deflected from the "cold" prediction due to relativistic thermal (finite-Larmor-radius) effects [12–14]. Qualitatively, such results have been observed also in full wave calculations [15, 16]. This phenomenon is usually called "anomalous" dispersion. Moreover, in specific cases the group velocity calculated from the standard Hamiltonian (i.e. the dispersion relation) can exceed the speed of light or become singular [17] (for example, this problem was met in Ref. [18], where it was corrected numerically by setting the limit). As was pointed out by Pilia and Fiodorov [19], Poynting's theorem in dissipative inhomogeneous media needs to be reconsidered since the classical formulation (see, e.g. Ref. [20]) contains a non-divergent loss term. A new definition of the power flux density and Hamiltonian which takes into account "anomalous" dispersion (Westerhof-Tokman model) was proposed in Refs. [21–23].

While the ray trajectory in almost all cases of practical interest can be calculated in the weakly relativistic or even "cold" approach, the resonance condition for calculating absorption (as well as emissivity and current drive) must be considered fully relativistically. Indeed, it can be easily found that the resonance interaction exists if the following condition is satisfied: $n\omega_{ce}/\omega \geq 1 - N_\parallel^2/2$ in the weakly relativistic and $n\omega_{ce}/\omega \geq (1 - N_\parallel^2)^{1/2}$ in the fully relativistic approaches (here, $\omega_{ce} = eB/m_e c$ is the cyclotron frequency, n is the harmonic number, and $N_\parallel$ is the parallel refractive index). The distance between the resonances found from the fully and weakly relativistic conditions, respectively, is about $|\Delta s| \sim (N_\parallel^4/8)L_B$ (here, $L_B \sim |d \ln B/ds|^{-1}$ is the characteristic scale of B variation). In the case of highly oblique launch in large scale devices, $|\Delta s|$ can be significant: for typical ITER param-

eters, it can reach 0.15 m.

In the ray- and beam-tracing codes, the common approach for calculations of electron cyclotron absorption, emissivity and current drive is the assumption that plasma response to the RF source remains linear, which is valid if the density of absorbed power, p_{abs}, is low compared with the rate of collisional thermalization, $p_{abs}/n_e T_e \nu_e \ll 1$ (here, n_e and T_e are density and temperature, respectively, and ν_e is the collision frequency for the resonant electrons). Since the typical ECRH/ECCD scenarios (especially in large machines) usually satisfy this condition, the electrons can be taken in calculations as Maxwellian. For an opposite case, the necessary numerical tools such as ray-tracing coupled with the Fokker-Planck solver have been successfully developed only for tokamaks (see, e.g. Refs. [24, 25]), while kinetic treatment of stellarators requires special attention. In particular, non-thermal effects in W7-AS with specific neo-classical convective flux due to the heating of trapped electrons were studied with help of the Fokker-Planck code FPTM [26, 27]. Generation of the spatial convective flux of trapped electrons by ECRH was confirmed also by Monte-Carlo simulations [28]. However, appropriate numerical solvers recognized as "standard" tools for stellarators are still absent.

One of the most important tasks for ray-tracing is to calculate current drive (CD). If the linear approach is valid, the most efficient method for calculating the current drive in plasmas is the adjoint technique [29], which only requires a Spitzer problem to be solved rather than a Fokker-Planck equation with a quasilinear diffusion term. Contrary to the Fokker-Planck solvers with bounce averaging (apart from FPTM), which can be applied only to axisymmetric plasmas, the adjoint technique is applicable for both tokamaks and stellarators. Under the assumption that only supra-thermal electrons contribute to the CD, this problem can be significantly simplified using the high-speed-limit (hsl) approximation [30–32], which has been used for a long time in many codes (see Ref. [33] and the references therein). However, the hsl model leads usually to underestimation of the CD efficiency (in some cases up to a factor of two) and is sufficiently accurate only for scenarios with high oblique launch of the RF beams or in plasmas with rather low electron temperatures. A necessity for a more accurate model with parallel momentum conservation (pmc) in like-particle collisions was clearly demonstrated in Refs. [33–35]. For this problem, a new rapid solver for the Spitzer problem with parallel momentum conservation was developed [35, 36], which calculates the CD efficiency with nearly the same accuracy as the Fokker-Planck solver (for ITER, discrepancy from CQL3D predictions is within a few percent [35]) .

Below, the code TRAVIS (TRAcing VISualized), a 3D ray-tracing code for microwaves of the electron cyclotron frequency range, is described. Starting from the first version of the code named BRT [37], TRAVIS was partly described in Refs. [34, 38] and [35]. The motivations for the development of the new ray-tracing code was the following. First of all, the tokamak-oriented codes listed in Ref. [33] exploit the axisymmetry of the magnetic equilibrium and cannot be directly applied to stellarators (at the moment, only three codes known to the authors can operate with 3D magnetic equilibria: TRECE [39], TRUBA [40] and ART [41]). Secondly, similarly to Refs. [22] and [42], the ray-tracing equations have to be formulated through the Westerhof-Tokman model which takes into account the thermal "anomalous" dispersion. Thirdly, the new code must use the adjoint technique with parallel momentum conservation in like-particle collisions, which is applicable for high temperature plasmas. Additionally, the code should also include an option for modeling ECE diagnostics with routines for estimating the theoretical limit of the spatial resolution for the ECE spectrum.

For better physics understanding, it is very instructive also to analyze the momentum-space information which can be extracted from the results. In particular, macroscopic quantities such as the deposition profile and the radiative temperature can be decomposed into contributions from trapped and passing electrons [37, 43]. This approach provides a better understanding of trapped-particle effects on heating, emission, and CD in stellarators, not only in interpreting the experiments, but also in preparing ECRH/CD scenarios. In addition, the energy range of the electrons responsible for absorption, emission and current drive can clarify the physics and applicability of used approaches.

The paper is organized as follows. In the second section, the physical models for ray-tracing, absorption, emissivity and current drive are described. In the third section, the structure of the code and the interface are presented. And, in the fourth, one examples of applications for ITER (as a benchmark) and the W7-X stellarator are shown.

2. Physical background and definitions

2.1. Ray-tracing equations

In the geometrical optics (GO) approach, the ray-trajectory can be defined as solution of the characteristic equations for $\mathcal{H}(\omega, \mathbf{k}; \mathbf{r}) = 0$ [12, 19],

$$\frac{d\mathbf{r}}{ds} = \frac{\partial \mathcal{H}}{\partial \mathbf{N}} \cdot \left| \frac{\partial \mathcal{H}}{\partial \mathbf{N}} \right|^{-1}, \qquad \frac{d\mathbf{N}}{ds} = -\frac{\partial \mathcal{H}}{\partial \mathbf{r}} \cdot \left| \frac{\partial \mathcal{H}}{\partial \mathbf{N}} \right|^{-1}, \quad (1)$$

where $\mathbf{r}$ is the radius-vector, $\mathbf{N} = \mathbf{k}c/\omega$ is the refractive index (for convenience, we use below both $\mathbf{k}$ and $\mathbf{N}$), s is the arc length along the ray, and $\mathcal{H}$ is the Hamiltonian. This form of equations is more convenient for calculations in comparison with the standard Hamiltonian equations [1, 2]) since the group velocity does not appear in Eq. (1) explicitly. Actually, the ray-trajectory is tangential to the power flux density [21–23],

$$\mathbf{S}(\omega, \mathbf{k}) = \frac{c|\mathbf{E}|^2}{16\pi} \frac{\partial \mathcal{H}}{\partial \mathbf{N}} \equiv \frac{|\mathbf{E}|^2}{8\pi} c \, \mathbf{F}(\omega, \mathbf{k}), \qquad (2)$$

where $\mathbf{E} = \mathbf{E}(\omega, \mathbf{k})$ is the complex amplitude of the wave electric field calculated as an eigenvector of the dispersion relation. $\mathbf{F}(\omega, \mathbf{k})$ is the dimensionless normalized power-flux density. The Hamiltonian can be represented in two alternative forms,

$$\mathcal{H} = \begin{cases} \mathcal{H}^{(1)} & = \mathrm{Re}(e_i^* D_{ij}^H e_j), \\ \mathcal{H}^{(2)} & = N^2 - N_\parallel^2 - [\mathrm{Re}(\mathcal{N}_\perp(\mathbf{k}))]^2, \end{cases} \quad (3)$$

where $D_{ij} = N^2 \delta_{ij} - N_i N_j - \epsilon_{ij}$ is the dispersion tensor, ϵ_{ij} is the dielectric tensor with superscripts H and aH denoting the Hermitian and anti-Hermitian parts, respectively, $N_\parallel$ and $N_\perp$ are the parallel and perpendicular parts of $\mathbf{N}$ with respect to the magnetic field, and $\mathbf{e} = \mathbf{E}/E$ is the wave polarization vector. Note that $N_\parallel$ and $N_\perp$ are the real solution of Eq. (1), while $\mathcal{N}_\perp$ is the complex solution of the wave's dispersion relation, $\|D_{ij}(\omega, N_\parallel, \mathcal{N}_\perp(\mathbf{k}))\| = 0$. Both Hamiltonians proposed, $\mathcal{H}^{(1)}$ in Ref. [21] and $\mathcal{H}^{(2)}$ in Ref. [22], contain the same physics and give practically the same numerical solutions [23]. It was found, nevertheless, that the form given by $\mathcal{H}^{(1)}$ is somewhat more convenient from a numerical point of view since it does not require solving the full dispersion relation, which itself is numerically non-trivial. In the particular case of the "cold" dielectric tensor in Eq. (3), both formulations produce the same solution.

Note also that for correctly taking into account the "anomalous" dispersion effects, the polarization vector, $\mathbf{e}$, must be calculated through the full dielectric tensor (the "cold" dielectric tensor is not sufficient). Since e_i and ϵ_{ij} appear only in a convolution, calculations can be done in the Stix reference frame [44] chosen in such a way that $N_x = N_\perp$, $N_y = 0$, $N_z = N_\parallel$.

The dielectric tensor, $\epsilon_{ij}(\omega, \mathbf{k})$, needed for calculating the Hamiltonian and the polarization in the code, is taken in the weakly relativistic approximation and represented in the form given in Ref. [45]. For recursive calculations applied for the Shkarovsky functions, the complex error function, $w(z)$, is required. In order to guarantee the accuracy needed for stable iterations, a new fortran-subroutine for $w(z)$ was written, which is based on a most precise (accuracy about 14 significant digits) and very rapid algorithm proposed in Ref. [46] (actually, this is an improved algorithm of Gautchi [47]). Optionally, for the Hamiltonian also the "cold" dielectric tensor can be used, which gives an acceptable accuracy for scenarios with sufficiently tenuous plasmas. In practice, for example, the "cold" model can always be used for O2- and X3-modes. In contrast, scenarios with O1- and X2-modes must be treated more carefully, especially for densities near the cut-off value, since the conditions for significant "anomalous" dispersion can be met.

For each given ray, the set of seven coupled equation (six ray-tracing equations Eq. (1) plus one for the optical depth, τ_ω, which is described in the next subsection) is solved in Cartesian coordinates using the package DLSODE [48]. The accuracy of tracing is controlled by setting "rel-ative accuracy options" of the ODE solver. Additionally, the Hamiltonian is kept small, $|\mathcal{H}| \lesssim 10^{-5}$. Strictly speaking, the Hamiltonian Eq. (3) must be zero, $\mathcal{H} = 0$, to ensure the solution with initially defined wave mode. Since the upper bound of the numerical error for $\mathcal{H}$ can be estimated as $|\Delta\mathcal{H}| \lesssim N^2$ with $|N| = \mathcal{O}(1)$, the value 10^{-5} is in fact the relative accuracy for the Hamiltonian.

In the present version of the code, both derivatives $\partial\mathcal{H}/\partial\mathbf{r}$ and $\partial\mathcal{H}/\partial\mathbf{N}$ in Eq. (1) are calculated numerically with the step sizes $\delta\mathbf{r}$ and $\delta\mathbf{N}$ chosen from the characteristic scales and condition $|\Delta\mathcal{H}| \ll 1$. While this approximation does not have any additional limitation for the "cold" model, for the weakly relativistic model, in the special case of quasi-perpendicular propagation near the relativistic cut-off point, the numeric derivatives may produce a large error due to the sharp peaking of the Shkarowsky functions. In other cases, i.e. far from the cut-off, the finite derivatives of the weakly relativistic Hamiltonian do not produce any significant error. This result has been supported by the benchmark against the WR_RTC code [49]. Furthermore, in most typical ECRH/ECCD scenarios for tokamaks and stellarators, where the kinetic effects in wave propagation are negligible, the "cold" Hamiltonian can be applied.

It is assumed that the original beam cross-section (from the gyrotron) is circular with a Gaussian power distribution. Each ray after beam discretization has the individual weight $w_r \propto \delta S_r\, e^{-2(\rho_r/\rho_b)^2}$, where ρ_r is the distance to the central ray, δS_r is the area "occupied" by the ray, and r is the ray index. After passing through the transmission-line, however, the shape of the beam cross-section can be transformed to elliptical. Considering the last launch mirror as the starting point for the beam, the initial conditions for the rays are defined as elliptical with arbitrary orientation and eccentricity (actually, two half-width are defined and the angle). Apart from this, a possible astigmatism is also included by defining two focal distances with respect to the ellipse axes.

From the antenna, each ray with the vacuum $|\mathbf{N}_0| = 1$ is taken to be straight up to the point of crossing the last closed magnetic surface (LCMS). At this point, the refraction index decomposed into the normal and tangential components with respect to the LCMS, $\mathbf{N} = \mathbf{N}_n + \mathbf{N}_t$, is obtained by iterations with N calculated from the cold dispersion relation for the desired wave mode in plasma and N_t from Snell's law, $N_t = \sin\theta_0$, where $\theta_0 = \cos^{-1}(\mathbf{n} \cdot \mathbf{N}_0)$ and $\mathbf{n}$ is the normal to LCMS.

For the given equilibrium, TRAVIS can handle several beams simultaneously and each beam is defined as an independent object with individual launch conditions, wave mode, approach for dielectric tensor, discretization, etc. This gives the possibility to calculate multi-beam scenarios by only one run without reloading the equilibrium that is useful for coupling with a transport code. In the case of an optically "gray" plasma with $\tau_\omega \sim 1$, i.e. if the single-pass absorption is less then 80%, reflections of shine-through power from the inner wall and mirrors can be included,

which makes it possible to investigate heating by beams with multiple passes. For this option, a file with data for the inner wall of the vessel and the mirrors must be included. Actually, due to error accumulation (depolarization, plasma outside the LCMS, which are not included in the model) only a few passes are physically meaningful.

In the present version of the code, the mode purity after reflection is assumed to be intact. Actually, this is not strictly true, but this assumption is approximately correct for the cases, when the point of re-entrance is located sufficiently close to the exit of the ray from plasma[1].

2.2. Absorption and deposition profile

As already was said before, the set of ray-tracing equations Eq. (1) is solved together with the equation for the optical depth,

$$\frac{d\tau_\omega}{ds} = \alpha_\omega, \qquad (4)$$

where α_ω is the cyclotron absorption coefficient, calculated in fully relativistic approach. This helps ODE solver to choose the appropriate integration step-size. All other necessary quantities are obtained then during integration from α_ω and τ_ω.

The key value for calculating the RF heating is the power absorption rate along the ray,

$$\frac{dP_{\text{abs}}}{ds} = P_0\, \alpha_\omega\, \mathrm{e}^{-\tau_\omega}, \qquad (5)$$

where P_0 is the initial power specified for each ray. Since each ray can cross the same magnetic surface more than once, the total deposition profile, $\delta P_{\text{abs}}/\delta V$, is reconstructed by summation of all ray contributions appeared in the plasma volume δV between the surfaces labeled by ψ and $\psi + \delta\psi$, respectively:

$$\frac{\delta P_{\text{abs}}}{\delta V} = \sum_{r,i} w_r \left| \frac{\delta s_{r,i}}{\delta V} \right| \left(\frac{dP_{\text{abs}}}{ds} \right)_{r,i}, \qquad (6)$$

where i enumerates the crossing of the layer δV by the ray with the index r, $\delta s_{r,i}$ is the arc-length of the ray trajectory which belongs to the elementary volume δV, and w_r is the initial "weight" of the ray.

Aside from the shape of the deposition profile, it is useful also to estimate its location together with its width. It can be easily done by introducing the moments of the deposition profile,

$$\overline{\rho_{\text{abs}}^m} = \frac{1}{P_{\text{abs}}} \cdot \int_0^{V_{\text{max}}} \rho^m \frac{\delta P_{\text{abs}}}{\delta V}\, dV, \qquad (7)$$

---

[1] A degradation of the mode purity in reflections can appear due to i) the depolarization on the corrugated surface and ii) the different magnetic field orientation at the points of exit and re-entrance. Since the option for multipass ray-tracing was originally oriented to the W7-X stellarator, where the special mirrors for reflection are provided and the points of exit and re-entrance are very close to each other, it is assumed that the mode purity is conserved, but not more than two reflections are accounted for.

where $\overline{\rho_{\text{abs}}}$ is the center of deposition (i.e. its location), $\delta\rho_{\text{abs}} = \sqrt{\overline{\rho_{\text{abs}}^2} - \overline{\rho_{\text{abs}}}^2}$ is its dispersion, i.e. the characteristic width of the deposition profile, $\rho = \sqrt{\Psi/\Psi_{\text{max}}}$ is the flux-surface label with Ψ as the toroidal magnetic flux, and $P_{\text{abs}} = \int_0^{V_{\text{max}}} (\delta P_{\text{abs}}/\delta V)\, dV$ is the total absorbed power.

Using the general definition for the absorption coefficient [4] $\alpha_\omega = (\omega/4\pi) E_i^* \epsilon_{ij}^{aH} E_j / |\mathbf{S}|$ (here, E_i is the wave electric field, ϵ_{ij}^{aH} the anti-Hermitian component of the dielectric tensor and $\mathbf{S}$ the wave power-flux density given by Eq. (2)), the expression for α_ω can be represented as the integral along the resonance line, defined by condition $\gamma - nY - N_\| u_\|/c = 0$ (here, $\gamma = \sqrt{1 + u^2/c^2}$ is the relativistic factor, $u = v\gamma$ is the momentum per unit mass, n is the harmonic number and $Y = \omega_{ce}/\omega$), which can be written for an arbitrary distribution function, f_e, as the 1D integral,

$$\alpha_\omega = -\frac{\pi\omega}{c^2\, |\mathbf{F}(\omega, \mathbf{k})|} \frac{\omega_{pl}^2}{\omega^2} \sum_n \int_{u_{\|,\min}}^{u_{\|,\max}} du_\| \left[\mathcal{D}_{ql}\, \hat{\mathcal{L}}(f_e) \right]_{\gamma = \gamma_{\text{res}}}, \qquad (8)$$

with the limits of integration, $u_{\|,\min}$ and $u_{\|,\max}$, being the solutions of the resonance condition $\gamma_{\text{res}} = nY + N_\| u_\|/c$ for $u_\perp = 0$. Here, $\hat{\mathcal{L}} = \frac{\partial}{\partial\gamma} + cN_\| \frac{\partial}{\partial u_\|}$ is the quasilinear differential operator, $\mathcal{D}_{ql} = (u_\perp/c)^2 |\mathbf{\Pi}_n|^2$ is the normalized quasilinear diffusion coefficient, $\mathbf{\Pi}_n = \mathbf{e}_- J_{n-1}(k_\perp \rho_e) + \mathbf{e}_+ J_{n+1}(k_\perp \rho_e) + \mathbf{e}_\| u_\|/u_\perp J_n(k_\perp \rho_e)$ with $k_\perp \rho_e = N_\perp u_\perp/cY$, and $\mathbf{e}_\pm = \mathbf{e}_x \pm i\mathbf{e}_y$ is the complex polarization vector. The upper resonance harmonic, which may participate in cyclotron interaction, is defined in the code by analyzing the magnetic equilibrium. In the present version of the code, the cyclotron interaction can be calculated up to 5th harmonic which is sufficient for any realistic scenario. In order to cut the tails of extremely energetic resonant electrons which produce only negligible contribution in cyclotron interaction if the electron distribution function is close to Maxwellian, the range of integration is limited by the choice $u \leq 7\, u_{\text{th}}$ with $u_{\text{th}} = \sqrt{2T_e/m_e}$.

Analyzing the integrand in Eq. (8), the energy range of electrons which make a contribution in absorption is defined (the energy which corresponds to half of the integral is the central, and the upper and lower values are estimated by analyzing the rest of the integral). Additionally, α_ω is decomposed into the contributions from passing and trapped electrons. This is done during integration of Eq. (8) by analyzing the normalized magnetic moment, $\lambda = u_\perp^2 B_{\max}/u^2 B$ (here, $B_{\max}$ is the maximum of the magnetic field at the given flux-surface), and splitting the integral into two parts for passing ($\lambda < 1$) and trapped ($\lambda > 1$) electrons. This option provides a better understanding of the relation between the power deposition and the current drive profiles [37, 43].

As the standard option, the distribution function f_e is

taken as normalized relativistic Maxwellian [50],

$$f_{eM}(u) = \left[\sqrt{\frac{\pi}{2\mu}} \, \frac{e^{-\mu}}{K_2(\mu)} \right] \frac{\mu^{3/2}}{\sqrt{2\pi}} \, e^{-\mu(\gamma-1)}, \qquad (9)$$

with $K_2(\mu)$ the modified Bessel function of second kind and $\mu = m_e c^2 / T_e$, which is sufficiently accurate for describing modern large-scale devices, where the power density is sufficiently low and no significant quasilinear distortion is expected. However, the formulations used in the code also allow for an arbitrary distribution function which opens a possibility to couple TRAVIS with any Fokker-Planck solver for considering particular scenarios with highly peaked deposition where significant quasilinear effects can be expected. It must be noted, however, that application of the non-Maxwellian in TRAVIS is not yet well benchmarked. At the same time, bi-Maxwellian distribution functions can be applied. This option has been tested already in the earlier version of the code for calculation of the high-field-side ECE-spectrum for W7-X [51].

2.3. Radiative temperature

In the ECE branch of the code, where the radiative electron temperature, T_{rad}, is calculated, the radiative transfer equation [2, 4]

$$N_r^2 \frac{d}{ds} \left(\frac{I_\omega}{N_r^2} \right) = \beta_\omega - \alpha_\omega I_\omega, \qquad (10)$$

is solved. Here, $N_r^2 = N^2 |\cos\vartheta \cdot \frac{d\Omega}{d\Omega_k}|^{-1}$ is the square of the ray refractive index [2, 52], $\cos\vartheta = (\mathbf{k} \cdot \mathbf{F})/kF$, $d\Omega$ and $d\Omega_k$ are the solid angles specified for the ray and the wave vector $\mathbf{k}$, respectively; β_ω is the emissivity and I_ω is the spectral radiation intensity which in the blackbody approximation can be expressed as $I_\omega = \omega^2 T_{\mathrm{rad}}/(8\pi^3 c^2)$. The radiation that reaches the antenna si discretized with respect to the antenna pattern. For tracing, it is assumed that each ray trajectory lies between the points of entrance of the ray into the plasma, $s = a$, and of exit, $s = b$ (in calculations, the trajectory with $a < s < b$ belongs to the plasma and the rest is in vacuum). Then the solution of Eq. (10) for the radiation at the exit-point can be represented as

$$I_\omega(b) = I_\omega^{inc} e^{-\tau_\omega^{ab}} + \int_a^b ds' \frac{\beta_\omega}{N_r^2} e^{-\tau_\omega(b) + \tau_\omega(s')}, \qquad (11)$$

where $\tau_\omega^{ab} = -\tau_\omega(a) + \tau_\omega(b)$ and I_ω^{inc} is the spectral intensity of the radiation incident on the plasma at the point $s = a$; boundary conditions require that $N_r(s = a, b) = 1$. For optically thick plasmas, when $\tau_\omega^{ab} \gg 1$, the contribution from the incident radiation can be neglected.

In the code, all trajectories are calculated in the direction opposite to the radiation, i.e. starting from the antenna through the point $s = b$ up to $s = a$ (typically, the trajectory is stopped earlier, at $\tau_\omega(s) = 10$). Then, following Eq. (11), the back integration, i.e. from a to b, is performed.

The radiative temperature is calculated by summation of the contributions from all rays coming to the antenna. Finally, following Kirchhoff's law for the blackbody emission, the radiative temperature can be written as

$$T_{\mathrm{rad}}(\omega) = \frac{8\pi^3 c^2}{\omega^2} \sum_r w_r I_{\omega,r}(b). \qquad (12)$$

However, if the frequency band-width for the ECE channel is large, T_{rad} must be calculated by averaging over the spectral width $\Delta\omega$ of the frequency channel ω_*,

$$T_{\mathrm{rad}}(\omega_*) = \langle g(\omega) T_{\mathrm{rad}}(\omega) \rangle_{\omega_* \pm \Delta\omega/2}, \qquad (13)$$

where $g(\omega)$ is the band-width function of a receiver with ω lying in the interval $\omega_* \pm \Delta\omega/2$ (typically, the rectangular model, $g(\omega) = 1$ is sufficient).

The emissivity β_ω which enters in Eq. (10) is defined in TRAVIS for an arbitrary distribution function in the same way as the absorption coefficient Eq. (8) [4, 53]:

$$\beta_\omega = N_r^2 \frac{m_e \omega^3}{8\pi^2 c^2 |\mathbf{F}(\omega, \mathbf{k})|} \frac{\omega_{pl}^2}{\omega^2} \sum_n \int_{u_{\parallel,min}}^{u_{\parallel,max}} du_\parallel \, [\mathcal{D}_{ql} f_e]_{\gamma=\gamma_{res}}, \qquad (14)$$

which for a Maxwellian distribution function satisfies Kirchhoff's law, $\beta_\omega/N_r^2\alpha_\omega = \omega^2 T_e/8\pi^3 c^2$. In order to minimize the computation time, the emissivity is calculated in the code together with the absorption coefficient. Analyzing then during the integration the complete integrand in Eq. (13), i.e. in $\sum_r w_r \langle g(\omega) I_{\omega,r}(s) \rangle_{\omega_* \pm \Delta\omega/2}$, also the spatial width of the emission line (i.e. theoretical limit of the spatial resolution) is calculated. To do this, the mapping to the flux-surface label is performed.

The energy spectrum of electrons which contribute into ECE radiation is estimated in the same manner as for absorption. This information is very helpful when it is necessary to distinguish the contribution from supra-thermal electrons. In particular, this information is required for analysis of the ECE spectrum obtained from oblique or high-field-side observation [38, 51].

2.4. Current drive

In this subsection, we omit general definitions related to the current drive and the adjoint technique and re-address the reader to Ref. [35], where all the necessary information and the references can be found.

Since the ratio $j_\parallel/B$ is constant on the magnetic surface (due to conservation of the current within the magnetic flux tube), the elementary toroidal current which circulates through the cross-section between the neighboring flux-surfaces ψ and $\psi + \delta\psi$ can be defined as follows:

$$\delta I_{\mathrm{tor}} = \int_\psi^{\psi+\delta\psi} \left(\frac{j_\parallel}{B} \right) \mathbf{B} \cdot d\mathbf{S} = \frac{\langle j_\parallel \rangle}{\langle B \rangle} \delta\Psi = \frac{\langle j_\parallel B \rangle}{\langle B^2 \rangle} \delta\Psi, \quad (15)$$

where $\langle j_\parallel \rangle$ is the parallel current-drive density, Ψ is the toroidal magnetic flux and $\langle ... \rangle$ means an averaging over the magnetic surface. Since the efficiency, $\eta = \langle j_\parallel \rangle / \langle p_{\text{abs}} \rangle$, but not directly $\langle j_\parallel \rangle$ is calculated in the ray-tracing codes, the current generated along the elementary arc-length of a ray is given by

$$\frac{dI_{\text{tor}}}{ds} = (\langle B \rangle V')^{-1} \, \eta \, \frac{dP_{\text{abs}}}{ds}, \qquad (16)$$

where dP_{abs}/ds is defined in Eq. (5). In the linear approach, which is assumed to be valid in the ray-tracing calculations, the CD efficiency does not depend on the absorbed power.

Summing up the contributions from all the rays similar to Eq. (6), the elementary toroidal current can be expressed as

$$\frac{\delta I_{\text{tor}}}{\delta \Psi} = \sum_{r,i} w_r \left| \frac{\delta s_{r,i}}{\delta V} \right| \left(\frac{dI_{\text{tor}}}{ds} \right)_{r,i}, \qquad (17)$$

and the value $\langle j_\parallel B \rangle$ can be calculated combining Eq. (15) and Eq. (17). The total toroidal current is given by the integral from the axis to the last closed flux-surface,

$$I_{\text{tor}} = \int_0^{\Psi_{\max}} (\delta I_{\text{tor}} / \delta \Psi) \, d\Psi. \qquad (18)$$

Similar to Eq. (7), it is meaningful also to define the "location" and the "width" of the current drive profile. Introducing the corresponding moments,

$$\overline{\rho_{\text{cd}}^m} = \frac{1}{I_{\text{tor}}} \cdot \int_0^{\Psi_{\max}} \rho^m \frac{\langle j_\parallel B \rangle}{\langle B^2 \rangle} \, d\Psi, \qquad (19)$$

the "center of CD profile", i.e. its location, $\overline{\rho_{\text{cd}}}$, is defined, and its dispersion, i.e. the "width" of the CD profile, $\delta \rho_{\text{cd}} = \sqrt{\overline{\rho_{\text{cd}}^2} - \overline{\rho_{\text{cd}}}^2}$.

For calculation of the current drive efficiency, η, the adjoint technique is applied (see Ref. [35] and the references therein), where the current drive is represented in terms of convolution of the RF source-term, $Q_{\text{RF}} = \hat{\mathcal{L}}[\mathcal{D}_{ql} \hat{\mathcal{L}}(f_{eM})]$, with the Green's function, $\chi(\mathbf{r}, \mathbf{u})$. Performing an integration along the resonance line similar to Eq. (8) and Eq. (14), the final expression for η at particular magnetic surface is

$$\eta = \frac{e u_{\text{th}} \langle b \rangle}{\nu_{e0} m_e c^2} \frac{\sum_n \int_{u_{\parallel min}}^{u_{\parallel max}} du_\parallel \left[\mathcal{D}_{ql} \hat{\mathcal{L}}(f_{eM}) \hat{\mathcal{L}}(\chi) \right]_{\gamma = \gamma_{res}}}{\sum_n \int_{u_{\parallel min}}^{u_{\parallel max}} du_\parallel \left[\mathcal{D}_{ql} \hat{\mathcal{L}}(f_{eM}) \right]_{\gamma = \gamma_{res}}}, \qquad (20)$$

where $\nu_{e0} = 4\pi n_e e^4 \ln \Lambda / (m_e^2 u_{\text{th}}^3)$ is the thermal collision frequency, $b = B/B_{\max}$ is the magnetic field normalized to its maximum on this magnetic surface, and χ is the generalized Spitzer function.

The efficiency defined in the adjoint technique by Eq. (20) automatically includes not only the Fisch-Boozer effect [30, 54], but also the effects related to the trapped particles, i.e. the Ohkawa effect [55] (asymmetry generated due to "pushing" of barely passing electrons by the RF source to the trapped/passing boundary) and drag over the trapped electrons [56]. All these effects can be decomposed in two parts: the linear contribution $\propto Q_{\text{RF}}(f_{eM})$ and the correction $\propto Q_{\text{RF}}(\delta f_e)$ due to the quasilinear distortion, $\delta f_e = f_e - f_{eM}$. The first of these, which is dominant (apart from rather exotic cases), can be calculated by both the Fokker-Planck and the adjoint techniques, while the second, which has a pure quasilinear nature, can be calculated only by the Fokker-Planck solver. Please note also that in the wake of Cohen's investigation [31], where the effect of the trapped electrons in ECCD, i.e. both the drag with trapped electrons and asymmetry of barely passing electrons, was studied by the adjoint technique (high-speed-limit was applied), the name "Ohkawa effect" is frequently used in the literature to describe general effects of the trapped electrons in the current drive.

The key point of the adjoint technique is a choice of the model which should correspond to the desired collisionality range with conservation of parallel momentum in the like-particle collisions and contains magnetic field, $B(\Psi, \theta, \varphi)$, without simplifications (here, θ and φ are the poloidal and toroidal angles, respectively). The simplest model corresponds to the high-collisionality limit with $\nu_e^* \to \infty$, when trapped particle effects produce a negligible contribution (here, $\nu_e^*(u) = \nu_e(u) R / \imath v$ is the collisionality, $\nu_e(u) = \nu_{ee}(u) + \nu_{ei}(u)$ is the electron collision-frequency, R and $\imath$ are the major radius and the rotational transform, respectively, and v is the electron velocity). This limit, which corresponds to the classical Spitzer problem, is included in the code only as a reference case for benchmarking purposes.

The opposite low-collisionality case with $\nu_e^* \to 0$ (also called "collisionless limit") is more relevant for the experimental conditions in fusion devices with high electron temperatures, where the contribution from the barely trapped electrons is negligible. The analytical expression for χ used in the code for this approach is the following [35]:

$$\begin{aligned}
\chi(u, \lambda; \sigma) &= \sigma H(\lambda) K(u); \\
H(\lambda) &= \frac{\langle b^2 \rangle}{2 f_c} h(1 - \lambda) \int_\lambda^1 \frac{d\lambda}{\langle \sqrt{1 - \lambda b} \rangle}; \quad (21) \\
f_c = 1 - f_{\text{tr}} &= \frac{3}{4} \langle b^2 \rangle \int_0^1 \frac{\lambda d\lambda}{\langle \sqrt{1 - \lambda b} \rangle},
\end{aligned}$$

where σ is the sign of $u_\parallel$, f_c and f_{tr} are the fractions of circulating and trapped particles, respectively, and $h(x)$ is the Heaviside function. The function $K(u) = \frac{3}{2} \int_0^1 d\lambda \, \chi(u, \lambda; \sigma = +1)$, which (apart from normalization) represents the generalized Spitzer function, is the solution of a 1D integro-differential equation [32, 57],

$$\widehat{C}_1^{\text{lin}}(K) - \frac{f_{\text{tr}}}{f_c} \nu_e(u) K(u) = -\nu_{e0} \frac{u}{\gamma u_{\text{th}}}, \qquad (22)$$

where $\widehat{C}_1^{\text{lin}}(K) \equiv C_1^{\text{lin}}(\chi_1 f_{eM}) / f_{eM}$ and C_1^{lin} is the 1st Leg-

endre harmonic of the linearized relativistic Coulomb operator.

Most important for a precise calculation of ECCD is the model chosen for the operator $\widehat{C}_1^{\mathrm{lin}}$. Historically, the high-speed-limit (*hsl*) model [31, 32] was commonly accepted as the standard for calculation of ECCD. This is very simple and convenient approach for numerical calculations, but in high-temperature plasmas the energy range of electrons, which make the main contribution to ECCD, is not so far from the bulk particle, $u_{res} < 3u_{\mathrm{th}}$ [35], and the *hsl* approach fails even for highly oblique launch. For TRAVIS, a very fast and sufficiently accurate numerical solver for Eq. (22) with parallel momentum conservation (*pmc*) has been developed [36] and benchmarked [35] (the results of benchmark are described in the subsection 5.2).

Recently, new approximate model for calculation of current drive with small but finite collisionality taken into account that is applicable for both tokamaks and stellarators has been developed [58, 59]. The applied approximation is based on the the momentum correction technique [60] and is partly benchmarked with respect to ECCD calculations against the NEO-2 code [61, 62] (despite the successful check of the main features for tokamaks, the benchmark is not yet fully completed). In this case, χ is given by

$$\chi(u, \lambda; \sigma) = \sigma H^{\mathrm{eff}}(\lambda; \nu_e^*) K^{\mathrm{eff}}(u), \qquad (23)$$

where the "off-set" model is applied for the pitch-dependence,

$$H^{\mathrm{eff}}(\nu_e^*; \lambda) = \frac{1}{f_c^{\mathrm{eff}}(\nu_e^*)} \left(f_c H(\lambda) + \frac{2}{3} h(1-\lambda) \delta f_c^{\mathrm{eff}}(\nu_e^*) \right) \qquad (24)$$

with $\delta f_c^{\mathrm{eff}} = f_c^{\mathrm{eff}} - f_c$, which is defined through the velocity-dependent "effective circulating fraction" of electrons, f_c^{eff}, which is equivalent to the mono-energetic parallel conductivity D_{33}, normalized by its Pfirsch-Schlüter value,

$$f_c^{\mathrm{eff}}(\nu_e^*(u)) = \frac{3\nu_e(u)}{2v} \frac{D_{33}(\nu_e^*(u))}{\langle B^2 \rangle}, \qquad (25)$$

where D_{33} is extracted from the data-base of mono-energetic transport coefficients pre-calculated by the code DKES [63].

Similar to $K(u)$, the generalized Spitzer function $K^{\mathrm{eff}}(u)$ is the solution of the equation

$$\widehat{C}_1^{\mathrm{lin}}(K^{\mathrm{eff}}) - \frac{f_{\mathrm{tr}}^{\mathrm{eff}}}{f_c^{\mathrm{eff}}} \nu_e(u) K^{\mathrm{eff}}(u) = -\nu_{e0} \frac{u}{\gamma u_{\mathrm{th}}} \qquad (26)$$

with $f_{\mathrm{tr}}^{\mathrm{eff}}(u) = 1 - f_c^{\mathrm{eff}}(u)$.

In TRAVIS, two options for solving Eqs. (22) and (26) exist: first is the numerical non-relativistic solver [60] and second is the weakly relativistic solver based on the variational principle with polynomial trial functions [36]. Both solvers cover the collisionality range from the collisionless limit to low-but-finite collisionality.

3. Magnetic equilibrium

All the calculations related to the magnetic equilibrium have been performed by the MConf library developed at IPP by one from the authors (Y.T.). The library provides all necessary geometrical quantities such as magnetic field, $\mathbf{B}$, fraction of trapped particles, f_{tr}, etc., and performs flux-surface averaging and coordinate transformations between magnetic and real space coordinates.

For operation with 3D magnetic equilibria, the file with Fourier spectrum for the set of magnetic surfaces is used. The equilibrium file must be pre-calculated by the VMEC code [64]. The formats needed for the input are VMEC wout-file or its derivatives with the Boozer coordinates produced by JMC [65] or similar codes. A tokamak 2D magnetic equilibrium is read from EFIT [66] output (EQDSK-file) and transformed to the tokamak symmetry flux-coordinates [67] with the Fourier representation similar to that of VMEC thus allowing the same interpretation.

To speed up consecutive calls of TRAVIS, for example from a transport code, MConf creates a 3D-mesh in cylindrical coordinates on which it tabulates the magnetic field $\mathbf{B}$, the flux-surface label S, etc., and provides functions for interpolation (here, $S = \Psi/\Psi_{\mathrm{max}}$ with the toroidal magnetic flux Ψ; optionally, also poloidal flux can be used). The mesh generator is parallelized using the multi-threading technique thus allowing exploitation of all cores of modern CPUs. Typical time needed for creating the mesh with 2 cm resolution in a poloidal cross-section and through 2 degree in a toroidal direction from the W7-X magnetic equilibrium in VMEC format is about 2 sec on a notebook with dual-core CPU at 2.5 GHz. The mesh along with the original magnetic equilibrium can be stored in a file for future use.

The TRAVIS code uses MConf library through a special interface module; this gives a possibility to plug-in another user library, which returns the magnetic field, Jacobian, creates the set of points belonging to the particular flux surface for performing flux-surface averaging, and provides a mapping from the real space coordinates to the flux-surface label.

All other quantities needed for TRAVIS are prepared by the interface module. This approach is very efficient for including TRAVIS as an ECRH module in any existing transport code (at present, TRAVIS is regularly used as a module in the IPP transport code [68]).

4. Structure of the code and interface

The code TRAVIS is provided in two versions, one for ECRH/ECCD calculations and second for ECE diagnostic. Both branches have a common part (tracing, magnetic equilibrium, plasma profiles, boundary vacuum-plasma, absorption, dielectric tensor modules and dispersion relation solver) and their specific modules (ECRH/ECCD branch: solver for Spitzer problem and calculation of ECCD profiles; ECE branch: solver for radiation-transfer
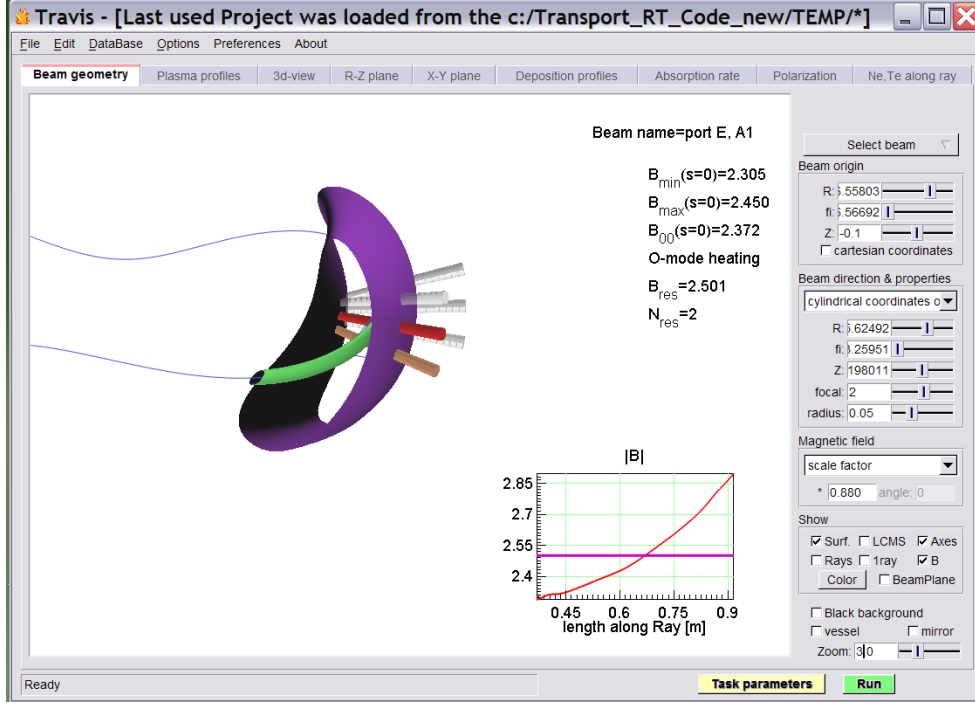
Figure 1: [color online] Example of the input-panel from the graphical interface of the TRAVIS code.

equation and calculation of the radiative temperature). The code can work as a stand-alone program as well as the module in another code (for example, in the transport code for updating the power deposition and current drive profiles).

In the ECRH/ECCD branch of TRAVIS, the task for calculations can be initialized in two ways, by direct definitions in the data-file and through a specially designed graphical user interface, which eases preparation of the input parameters together with very helpful presentation of the geometry in convenient (2D and 3D) form. In particular, the start location and direction of any beam (the code allows definition of several independent beams simultaneously) are immediately shown together with the magnetic equilibrium in 3D view being convenient for a fast choice of the relevant parameters. In Fig. 1, an example of the ECRH configuration for the W7-X stellarator is shown. Generally, several beams are under consideration, and the user can alter data for any beam by making appropriate changes (the selected beam, parameters of which are defined in the right-part of the panel, is marked by the color red).

The plasma profiles, $n_e(\rho)$, $T_e(\rho)$ and $Z_{\rm eff}(\rho)$, can be defined reading data stored on the grid or, as an alternative, analytically. The analytical definitions are represented by the general formulae,

$$f(\rho)/f_0 = g - h + (1 - g + h)(1 - \rho^p)^q + h(1 - e^{-\rho^2/w^2}), \quad (27)$$

with the set of five parameters, shown at the screen: f_0 is the value on axis, $g = f(1)/f_0$ is the normalized boundary value, p and q are the powers for parabolic dependence, h is the magnitude of an axial "hole" of the width w (the last two parameters are useful for description of "hollow" density profiles possible for stellarators).

The other parameters, which can be defined through the graphical interface are the number of rays applied for discretization, the definition of the beam-cone, the model for the dispersion relation ("cold" or weakly relativistic), the accuracy for ODE-solver, etc. All these parameters are individual for each beam.

The major part of a calculation's results is shown graphically (in other tabs, see Fig. 1) and also written to files. There is the local information along each ray trajectory like $N_{\perp,\parallel}$, n_e, T_e, B, $\rho = \sqrt{S}$, etc., and the integral values and profiles like $P_{\rm abs}$, $I_{\rm tor}$, etc. Together with the standard output of values like $dP_{\rm abs}/ds$, $dI_{\rm tor}/ds$, $dP_{\rm abs}/dV$, the contributions of passing and trapped electrons are shown. Apart from this, an evolution of the polarization vector is shown (both the real and imaginary parts of e_x, e_y and e_z). For comparison, the polarization can be shown in the "cold" as well as in the weakly relativistic approaches. The importance (or its negligible weight) of the "anomalous dispersion" can be estimated from the plotted cosine between the wave vector and the power flux, i.e. $\cos \angle = \mathbf{k} \cdot \mathbf{F}/kF$ (see Eq. (2)). Additionally, the energy range of the resonant electrons which produce the main contribution in absorption, emission and current drive is shown along the trajectory of the central ray. This information is very helpful for a deeper understanding of the process.

8

The core of the code is written in fortran-90 in such a way that the beams and corresponding rays are described by their own structures, declared as derived types, and the code itself does not contain any static variables. This object-like style eases the parallelization of the code which is important for including it in the real-time ECE diagnostic software. At present, the code is not parallelized, but this can be easily done.

5. Benchmark and applications of the code

Since only the model for current drive calculations is completely new in comparison with other codes, benchmarking has been separated into two parts: 1) testing the ray trajectory and absorption profile, and 2) testing the current drive calculations. A several very different scenarios were considered.

5.1. Tracing and absorption

If the electron temperature is high enough, the preferable model for calculation of absorption is the fully relativistic approach (in TRAVIS, this option is default). For the Scenario-2 in ITER [69] and for the upper launcher conditions [33], calculations of the ray trajectories with the "cold" Hamiltonian were performed, while the absorption was calculated with both weakly relativistic and fully relativistic models. It was found that the locations of dP_{abs}/ds for both weakly and fully relativistic approaches are practically the same as obtained by the code GRAY [8] (see also [33]). However, the shift between the "cold" profile and weakly relativistic (i.e. more precise) profile does not change drastically the general picture. At the same time, there are scenarios where accuracy of the model is more important. For example, for the equatorial launcher in ITER with the toroidal launch angle 30° ($N_\parallel \simeq 0.64$ in the absorption region), the fully relativistic resonance appears at the ray trajectory about 18 cm before the weakly relativistic one, resulting in a shift of the deposition profile $\Delta\rho \simeq 0.044$ towards off-axis and 23% reduction of dP_{abs}/dV at maximum.

The benchmarking of "cold" ray-trajectories and the depositions profiles was done also against TORBEAM [11]. For this purpose, ASDEX-Upgrade conditions were applied and very good agreement was obtained. For a 3D stellarator equilibrium, the code was successfully benchmarked against the code TRECE [39] ("cold" tracing and weakly relativistic absorption) for conditions of the Heliotron-E device [70].

The cases where "anomalous" dispersion induced by the thermal effect can be significant were tested for the ITER Scenario-2 mentioned above. For calculations, the Westerhof-Tokman Hamiltonians Eq. (3) with both the "cold" and weakly relativistic dielectric tensor were applied and compared with results from the WR_RTC code [49]: the agreement was found to be satisfactory.

For demonstration an importance of the "anomalous" dispersion, calculations were performed for quasi-vertical
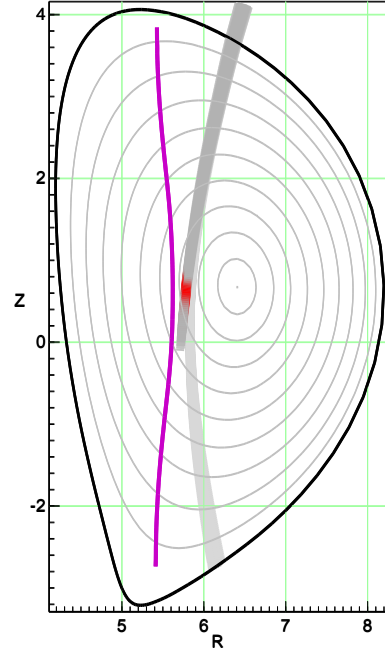

Figure 2: [color online] Quasi-vertical injection from the upper launcher in ITER. The beam that completely absorbed near the resonance line (shown by thick line) is calculated with the "cold' Hamiltonian. The beam that shines through without absorption is calculated with weakly relativistic Hamiltonian.

injection from the upper launcher in ITER. In Fig. 2, the ray trajectories of RF beams (O1 mode) in the RZ plane calculated with the different Hamiltonians are shown. The starting point for the central ray is $R = 6.485$ m and $Z = 4.11$ m and the launch angles are $\alpha = -74°$ and $\beta = 18°$. The rays calculated using the "cold" Hamiltonian are completely absorbed in the region near the cyclotron resonance. Due to the Doppler shift ($N_\parallel \simeq 0.25$ near the resonance), the condition for cyclotron interaction is met before crossing the surface $\omega = \omega_{ce}$. However, the rays calculated with weakly relativistic Hamiltonian experience a bending from the "cold" trajectories near the cyclotron resonance. Furthermore, even small change of the trajectory and $N_\parallel$ leads to losing of cyclotron resonance and no absorption appears. Physically, these results are very close to those that were obtained for TCV [13] and JET [14].

5.2. ECCD in ITER

The benchmark of numerical tools for current drive calculations requires special attention. For calculation of the current drive efficiency, two collisionless models based on Eqs. (21) and (22) were applied: Spitzer-problem solvers for the high-speed-limit (hsl) [32] and for the parallel-momentum-conservation (pmc) approaches [36]. Again, we follow the line proposed for benchmarking of the different beam/ray-tracing codes [33] and consider the same ITER scenario.

Using the scenario with the beam from the equatorial launcher in ITER, an angle-scan was performed and compared with the results obtained by the TORAY and CQL3D
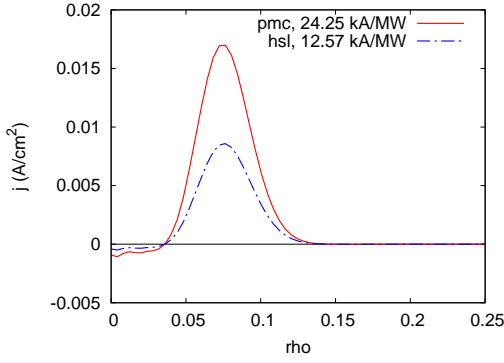
9

Figure 3: [color online] ECCD profiles in Gedankenexperiment for ITER, calculated with `TRAVIS` with the different approaches: solid line - *pmc*, and dashed-dot line - *hsl*. (Compare with Fig. 12 in Ref. [33])
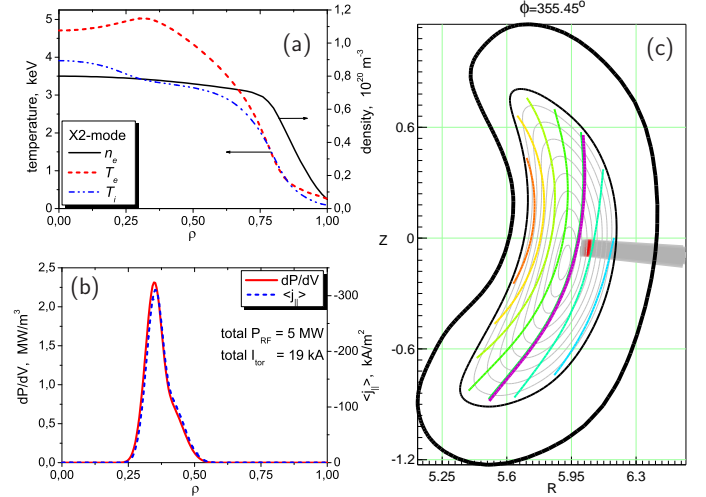

Figure 4: Results for X2-scenario in W7-X. (a) plasma profiles calculated by coupled 1D transport code and `TRAVIS`; (b) deposition and current drive profiles obtained by adding results for the five oblique beams launched from different ports; (c) the ray trajectories in the RZ-plane for one beam (magnetic surfaces and B-isolines with magenta at $\omega = 2\omega_{ce}$ are shown).

codes. The results of calculations with the *hsl* model coincide well with those calculated by the code `TORAY`, while the results from the more precise *pmc* model are in good agreement with the Fokker-Planck solver `CQL3D`. For the angles checked, the maximum discrepancy between the currents calculated with the different models, *hsl* and more precise *pmc*, is about 20%, i.e. *hsl* significantly underestimates the current drive [35].

In order to demonstrate an importance of parallel momentum conservation in current drive calculations, R. Prater proposed [33] the gedankenexperiment for ITER with the moderate launching angle (12.3° from radial) and location of the EC resonance quite close to the magnetic axis. In these conditions the counteracting effect from the trapped electrons is reduced due to the smallness of $f_{\rm tr}$, and bulk electrons are responsible for generation of the current owing to moderate $N_{\parallel}$. It was found that the *hsl*-model gives approximately half of the current obtained with the Fokker-Planck calculations (see Fig. 12 in Ref. [33]). In Fig. 3, the results of the same calculations performed by `TRAVIS` with both the *pmc* and *hsl* models are shown. Similar to the Fokker-Planck calculations [33, 35], the current drive obtained with the relativistic *pmc* model is higher than that obtained with the *hsl* by a factor of two. The reason for so strong ECCD underestimation is that mainly the electrons with $u_{\rm res} \sim 1.5 u_{\rm th}$ are responsible for the current drive generation, which is clearly outside the applicability of the high-speed-limit. The results of the benchmark against `CQL3D` shown in Ref. [35] clearly demonstrate that the *pmc* model [36] developed for `TRAVIS` is more adequate than *hsl* for the simulation of ECCD scenarios in high-temperature plasmas.

5.3. W7-X Stellarator: X2-scenario

Let us consider the typical ECRH/ECCD scenario in the W7-X stellarator with the X2-mode at 140 GHz (for details see Ref. [43]). This scenario is most acceptable for low and moderate plasma density. If the mode-purity is sufficiently high, optical depth is high, $\tau_{\rm X2} \gg 1$, and complete

single-pass absorption is expected. The deposition profile accounting for both Doppler broadening and relativistic effects is well localized and quite predictable. The following scenario was simulated: five oblique RF-beams of 1.0 MW each were launched from different ports. The "standard" magnetic configuration optimized for small neoclassical transport [71] was used. The magnetic field on axis was chosen to be 2.56 T (the "resonance" value is 2.5 T) in order to have the deposition profile shifted in the low-field-side direction (this is desirable if the X2-scenario is applied as the pre-heating scenario before subsequently switching to the O2-scenario). The launch-ports are situated near the "bean-shaped" plane where the maximum of B is located (in the "standard" magnetic equilibrium of the W7-X stellarator, the variation of magnetic field strength along the axis is $B_{\rm max}/B_{\rm min} = 1.09$) so as to guarantee a minimization of heating of the trapped electrons.

In these calculations, the density profile with $n_e(0) = 0.8 \times 10^{20}$ m^{-3} and the effective charge (uniform with $Z_{\rm eff} = 1.5$) were assumed to be fixed. The plasma temperatures (see Fig. 4(a)) were calculated by the 1D transport code [68] coupled self-consistently with `TRAVIS`. Calculations were done under the assumption that the neoclassical transport dominates in the plasma core while the anomalous transport acts in the periphery of the plasma. In Fig. 4(b), the deposition and ECCD profiles summarized for all five beams are shown. Since all beams are launched approximately with the same angles, the total deposition profile is localized quite well. As expected, the location and the shape of the total current drive coincides well with the power deposition profile.

As an example, in Fig. 4(c), also the ray trajectories of one of the five beams are shown (*RZ*-plane at toroidal angle that corresponds to the maximum of deposition). The
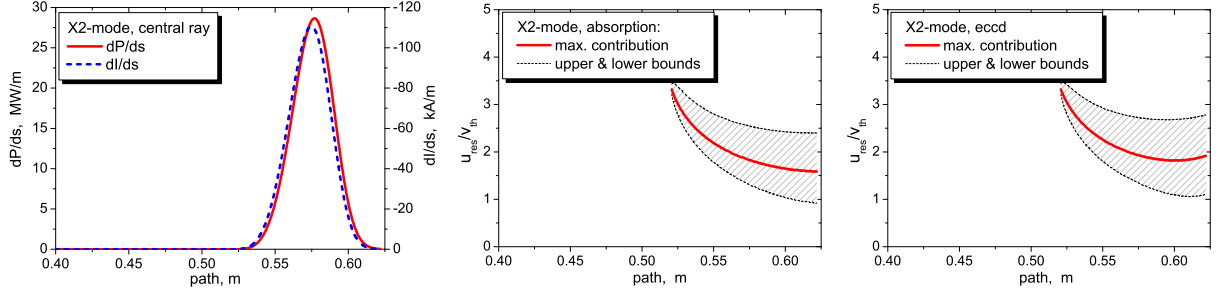
Figure 5: [color online] Results for X2-scenario, evolution along the central ray. Left: dP_{abs}/ds and dI_{tor}/ds. Middle and right: momentum range of electrons contributing in absorption and the current drive, respectively.

beam with Gaussian distribution of power was discretized into 41 rays. Single-pass absorption of the X2-mode for these plasma parameters is complete and the RF-power is absorbed somewhat before the resonance plane, $\omega = 2\omega_{ce}$ (the toroidal launch angle is about $20°$ and $N_\parallel \simeq -0.25$).

It is interesting to consider the results for this beam in detail. In Fig. 5, left, the evolution of dP_{abs}/ds and dI_{tor}/ds (see Eqs. (5) and (16), respectively) along the central ray are shown. Here, current drive was calculated with the weakly relativistic pmc-model. One can see that the current drive profile almost reproduces the shape of the absorption rate. This can be easily explained by a few factors. First of all, the plasma is optically thick for the considered scenario and only passing electrons with $k_\parallel v_\parallel > 0$ are involved in the cyclotron interaction. Secondly, despite the strong dependence of the Spitzer function on the energy, the momentum range of the electrons contributing to current drive does not change significantly in the absorption area. One can see this clearly from Fig. 5, middle and right, where an evolution of $(u/u_{\mathrm{th}})_{\mathrm{abs,cd}}$ is shown (the red lines correspond to the half values of the integrals along the resonance line and the shadowed area shows the range where 90% of the integral is reached, i.e. the wings with 5% of contribution from both sides are cut off in the figure). Indeed, in the area where the absorption happens (between the points in trajectory 0.55 m and 0.6 m) the main contribution in current drive is coming from the electrons with $(u/u_{\mathrm{th}})_{\mathrm{cd}} \simeq 2$, and the efficiency (not shown here) does not have any significant change. Again, this demonstrates clearly why the high-speed-limit for the adjoint technique is not generally suitable for calculation of ECCD: here the momentum range for current drive surely does not satisfy the necessary condition for applicability of the hsl approach.

5.4. W7-X Stellarator: O2-scenario

Contrary to the X2-scenario, where single-pass absorption is 100% and the deposition profile is defined predominantly by the magnetic field and obliqueness of the beam, the O2-scenario is more complex. First of all, for typical plasma parameters the plasma is optically gray ($\tau_{\mathrm{O2}} \sim 1$) and single-pass absorption is about 60-80%. In order to

prevent the uncontrolled depolarization of the reflected RF-beam, corrugated mirrors which save the desired polarization in the reflected beam are installed at the inner wall. Usually, after two passes through the plasma about 90% of the power is absorbed and the remaining power can be somewhat depolarized during reflection from the wall before the third pass through the plasma. Nevertheless, in calculations we consider the third pass with the same polarization since this approximation only weakly affects the final results.
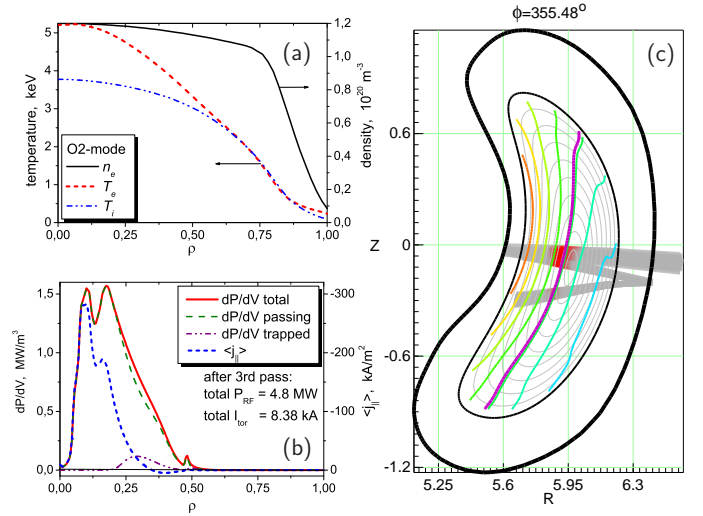

Figure 6: [color online] The same as in Fig. 4 for the O2-scenario. The beam has two reflections: first - from the inner mirror, and second - from the wall.

Due to a nonlinear dependence of the absorption coefficient on the electron temperature [4], the optical depth approximately scales as $\tau_{\mathrm{O2}} \propto T_e^2$ (this dependence is rigorous only for plasmas with well-localized absorption). As a consequence, the O2-scenario cannot be applied as the start-up scenario and needs a stage of pre-heating. Considering the X2-scenario described in the previous subsection as the pre-heating scenario, after reaching the steady-state and changing polarization from X- to O-mode with the same launch conditions (the beams must be directed to the mirrors), we discuss below the results of mod-
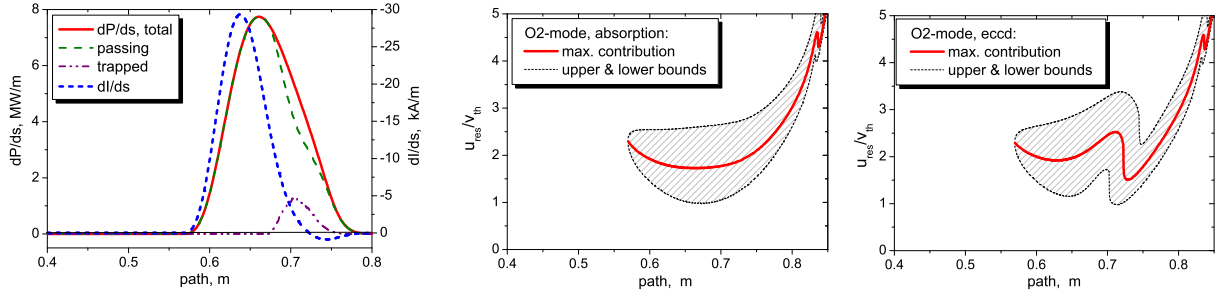
11

Figure 7: [color online] The same as in Fig. 5 for the O2-scenario. Additionally, at the left the deposition profile is shown for both the passing and trapped electrons.

elling of the O2-scenario with the density increased to $n_e(0) = 1.2 \times 10^{20}$ m^{-3}. Keeping in mind also that plasma pressure is already not negligible, the magnetic equilibrium was calculated by VMEC for the same vacuum field, but with $\beta = 2\%$ (here, $\beta = 8\pi p/B^2$ with $p = n_e T_e + n_i T_i$).

The temperature profiles (see Fig. 6(a) are calculated in the same manner as before, i.e. by the 1D transport code coupled with TRAVIS. Note that contrary to the X2-scenario, in this case the deposition profile (see Fig. 6(b)) is almost on-axis despite of the same value of vacuum magnetic field. This happens due to reduction of the magnetic field owing diamagnetic effects and Shafranov shift. Additional effect is the high sensitivity of the rate of absorption from the electron temperature. As a result, the temperature profile is peaked on axis (compare with the flat profile in the case of the X2-scenario, considered above) being well linked with the obtained deposition profile. Since a single-pass absorption for the considered scenario is about 80%, three passes were taken into account and only 4% of the launched power is unabsorbed (because of uncontrolled depolarization and absence of exact conditions for further reflections, there is no sense to increase the number of passes). An example for the same beam as in Fig. 4 is shown in Fig. 6(c) where the trajectories are projected onto the RZ-plane of the maximum of deposition for the first pass.

Since the structure of the deposition and current drive profiles is much more complex in comparison with the X2-scenario, let us consider it in detail. In Fig. 7(b) one can see that power is absorbed not only by passing electrons, but a small fraction from the trapped electrons appears. The deviation of the current drive profile is much more pronounced, where even the negative contribution appears. As a result, the total toroidal current for the same launched power is more than a factor of two smaller in comparison with the X2-scenario. This can be explained as follows. As seen in Fig. 7(b), the width of deposition is about 20 cm (compare with 6 cm for X2-scenario) and the resonance condition is changing along trajectory much stronger. In particular, near the point 0.67 m on the trajectory, the point $\omega = 2\omega_{ce}$ is crossed and near this point the Ohkawa effect becomes to be significant. Moreover,

starting from this point the contribution from electrons with $k_\parallel v_\parallel < 0$ appears which drives the current with opposite sign. Apart from this, the trapped electrons which already participate in absorption do not produce any current drive. As a consequence, dI_{tor}/ds starts to drop well before dP_{abs}/ds and even changes the sign where the contribution of electrons with $k_\parallel v_\parallel < 0$ becomes dominant. The effect of absence of contribution from the trapped electrons is perfectly seen in Fig. 7 (middle and right), where the momentum range of electrons responsible for ECCD is drastically different from the same for absorption.

5.5. W7-X Stellarator: ECE-diagnostic

The standard scheme of low-field-side (LFS) ECE measurements is based on two conditions. The first is a high optical thickness of plasmas for the observed frequency of the radiation. Usually, this is well satisfied (apart from the outer radii) for the frequency range which corresponds to the X2-mode and partly for the O1-mode. The second condition is the assumption that the electron distribution function is Maxwellian. The formal condition for this is the smallness of quasilinear effects induced by the RF source, i.e. smallness of the absorbed power density with respect to the thermalization rate, $p_{abs}/(n_e T_e \nu_e) \ll 1$, which is usually true apart from the scenario with an extremely highly peaked deposition profile in the low-density discharge.

The main contribution in ECE observed from the LFS is produced by the electrons which belong to the bulk where any deviation from Maxwellian is expected to be small. The detection of non-thermal effects requires a special technique and a high-field-side (HFS) observation is estimated to be very sensitive to the presence of a nonthermal population of electrons [72, 73]. There was shown that contrary to emission which is a local characteristic, the energy range of electrons, which are responsible for the re-absorption, is defined exactly by the direction of observation being quite different for LFS and HFS cases. Respectively, the down-shifted emission of energetic electrons, which propagates in the direction of increasing B is not reabsorbed and can be identified in the measurements. An applicability and attractiveness of the HFS measurements for W7-X has also been proved by ray tracing [51]
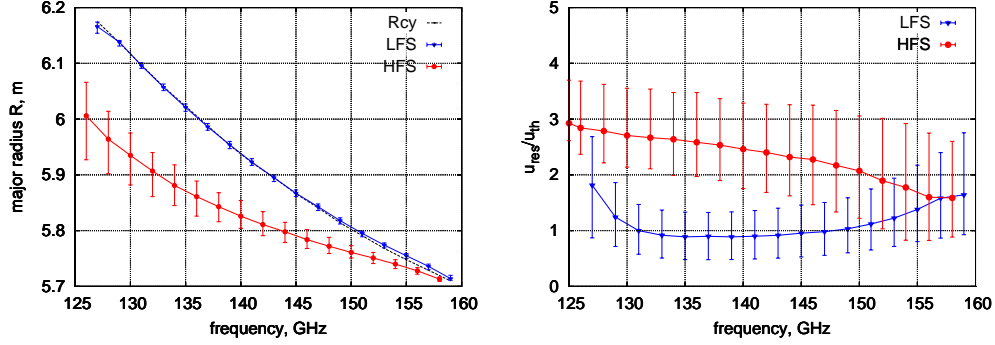
12

Figure 8: [color online] Left: The major radius (axis y) corresponding to the location of ECE *vs* the frequency (axis x) shown together with the spatial resolution. Both the LFS and HFS spectra are shown. The location of "cold" resonance at the vacuum sight-line is shown by black/dashed line. Right: the momentum of resonant electrons which contribute in ECE are shown for the same frequencies.

and for this purpose an additional ECE antenna is planned for the inboard side of W7-X [74].

The ECE diagnostic designed for W7-X is based on LFS measurements of the X2-mode near the "bean-shaped" plane where ∇B is largest (for details, see Ref. [74] and the references therein). Since the sight-line is quasi-perpendicular to the magnetic field (in vacuum, $86° < \theta < 92°$) and the Doppler effect is sufficiently small, the spatial resolution is defined by the relativistic broadening. The same sight-line must also be used for auxiliary HFS measurements. An example which illustrate the ECE for both LFS and HFS is calculated for $B = 2.5$ T on axis, which correspond to the frequency range for X2-mode, and for plasma with $n_e(0) = 0.8 \times 10^{20}$ m^{-3} and $T_e(0) = 6$ keV.

In Fig. 8 (left), the location of the ECE-line together with its spatial resolution is shown: the major radius corresponds to the region from where the emission of the given frequency is coming. Additionally, the location of the "cold" electron cyclotron resonance at the vacuum sight-line is shown. One can see, that due to strong reabsorption, the emission observed from the LFS is coming for each frequency from the region very close to the "cold" resonance position. And, *vice versa*, emission observed by the HFS antenna, originates from the regions of the plasma significantly shifted inside. Although the results of HFS observation seem like for optically gray plasmas, where the width of the emission line for the given frequency is rather broad, this circumstance actually reflects only the fact that the emission is coming from the region with suppressed reabsorption.

As seen in Fig. 8 (right), the momentum range of the resonant electrons which contribute to ECE for both LFS and HFS is separated well. Due to strong reabsorption, the bulk electrons with $u/u_{\text{th}} \simeq 1$ are responsible for the LFS spectrum. But for the HFS, more energetic electrons, $u/u_{\text{th}} \sim 2-3$, contribute to the emission, allowing the possibility to identify appearance of supra-thermal electrons due to quasilinear effects.

6. Summary

The ray-tracing code `TRAVIS` has been developed for electron cyclotron studies with emphasis on heating, current drive (CD) and ECE diagnostic. The code works with an arbitrary 3D magnetic equilibria and is thus applicable for both stellarators and tokamaks.

Due to a general model for the Hamiltonian, the kinetic effects which lead to anomalous dispersion are taken into account. Macroscopic quantities such as the deposition profile or the radiative temperature can be decomposed into the contributions from trapped and passing particles. This tool provides a better understanding of the kinetics of ECRH and ECCD, being not only useful in interpreting experiments, but also as a predictive means of designing plasma discharges. The spatial width of the emission line, calculated together with the ECE spectrum, gives the theoretical upper limit to the spatial resolution of the ECE diagnostic. The energy range of emitting electrons calculated gives an additional possibility to analyze kinetic effects.

Special attention in development of the code was devoted to the model for current drive calculations. The model is based on the adjoint technique in the collisionless limit with the Spitzer function obtained with parallel momentum conservation in electron-electron collisions. The accuracy of the numerical tools for obtaining the Spitzer function in both the weakly relativistic approach and the fully relativistic approach is sufficiently high as confirmed by benchmarking against the Fokker-Planck solver. It needs to be stressed that these numerical tools for calculations of the current drive remain not only sufficiently simple and fast but also significantly more accurate and adequate to modern fusion devices than the high-speed-limit model.

The code has been well benchmarked against the 3D code `TRECE`, the tokamak codes `TORBEAM`, `GRAY` and `WR_RTC` (with the last, "anomalous" dispersion was benchmarked). Additionally, the code was successfully tested with the ITER reference scenario-2 against predictions collected by R. Prater [33] (the results of this benchmarking were not

13

included therein but partly published later [35], where the current drive efficiency with parallel momentum conservation was calculated and compared with the Fokker-Planck calculations by `CQL3D` code).

The code is used through a specially designed graphical user interface, which allows the preparation of input parameters and viewing results in a convenient form. The aim of this interface, where the definition of input data as well the choice of output options can be done by clicks, is to make the code suitable and comfortable for any interested user. The major part of results is shown graphically: 2D and 3D figures for the magnetic equilibrium and the rays therein, the local information along each ray trajectory, the integral values like P_{abs}, I_{tor}, etc. Together with the standard output of the values like dP_{abs}/ds, dI_{tor}/ds, dP_{abs}/dV, the contributions from passing and trapped electrons are shown.

The code is routinely exploited now in both a stand-alone version and coupled with a 1D transport code [68] in modeling of heating and current drive scenarios at various harmonics of the ordinary and extraordinary mode (O1, O2, X2 and X3) [43, 75–77] as well as in modeling of the ECE diagnostic in the different W7-X magnetic equilibriums [38, 51, 74]. The code is also used to support the design of ECRH launcher components for W7-X [78]. Additionally, the code is already in use for ECRH and ECCD research in such devices as LHD [79, 80] and Heliotron-J [81].

Acknowledgement

References

[1] V. L. Ginzburg, *Propagation of Electromagnetic Waves in Plasma* (Gordon and Breach, Science Publishers, Inc., New York, 1961).

[2] G. Bekefi, *Radiative Processes in Plasmas* (John Wiley & Sohn, New York, 1966).

[3] Y. A. Kravtsov and Y. I. Orlov, *Geometrical optics of inhomogeneous media* (Springer-Verlag, Berlin, New York, 1990).

[4] M. Bornatici, R. Cano, O. de Barbieri, and F. Engelmann, Nucl. Fusion **23**, 1153 (1983).

[5] J. Arnaud, Applied Optics **24**, 538 (1985).

[6] E. Mazzucato, Phys. Fluids B **1**, 1855 (1989).

[7] G. V. Pereverzev, Phys. Plasmas **5**, 3529 (1998).

[8] D. Farina, Fusion Sci. Technol. **52**, 154 (2007).

[9] A. A. Balakin, M. A. Balakina, G. V. Permitin, and A. I. Smirnov, Plasma Phys. Reports **33**, 337 (2007).

[10] K. Matsuda, IEEE Trans. Plasma Sci. **17**, 6 (1989).

[11] E. Poli, A. G. Peeters, and G. V. Pereverzev, Comp. Phys. Comm. **136**, 90 (2001).

[12] E. Mazzucato, I. Fidone, and G. Granata, Phys. Fluids **30**, 3745 (1987).

[13] A. Pochelon *et al.*, in *Proc. 20th EPS Conf. on Control. Fusion and Plasma Phys., Lisboa (1993), Vol.17C, part III* (IAEA, Lisboa, 1993), p. 1029.

[14] H. Bindslev, in *Proc. 9th Joint Workshop on ECE and ECRH, Borrego Springs, California, USA, January 1995* (World Scientific, Singapore, 1995), p. 585.

[15] D. C. McDonald, R. A. Cairns, C. N. Lashmore-Davies, and G. L. Clair, Phys. Plasmas **5**, 883 (1998).

[16] M. A. Gavrilova and M. D. Tokman, Plasma Phys. Reports **24**, 529 (1998).

[17] V. V. Alikaev, A. G. Litvak, E. V. Suvorov, and A. A. Fraiman, in *High-Frequency Plasma Heating*, edited by A. G. Litvak (American Institute of Physics, New York, NY 10017-3483, 1992), p. 1.

[18] G. L. Clair, I. P. Shkarofsky, Y. Demers, and J.-F. Mercier, Relativistic Electron Cyclotron Ray-Tracing, preprint CCFM RI 472e, June 1997.

[19] A. D. Pilia and V. I. Fiodorov, in *Reviews of Plasma Physics*, edited by B. B. Kadomtsev (Consultant Bureau, New York – London, 1984), Vol. 13, p. 335.

[20] V. M. Agranovich and V. L. Ginzburg, *Spatial Dispersion in Crystal Optics and the Theory of Exitons* (John Wiley & Sons, Ltd., London, New York, Sydney, 1966).

[21] A. I. Smirnov and M. D. Tokman, Sov. Phys.-JETP **83**, 294 (1996).

[22] E. Westerhof, Plasma Phys. Control. Fusion **39**, 115 (1997).

[23] M. D. Tokman, E. Westerhof, and M. A. Gavrilova, Plasma Phys. Control. Fusion **42**, 91 (2000).

[24] R. W. Harvey *et al.*, Phys. Fluids B **5**, 446 (1993).

[25] Y. Peysson and J. Decker, AIP Conf. Proc. **1069**, 176 (2008).

[26] N. Marushchenko, U. Gasparino, H. Maaßberg, and M. Romé, Comp. Phys. Comm. **103**, 145 (1997).

[27] M. Romé *et al.*, Plasma Phys. Control. Fusion **39**, 117 (1997).

[28] S. Murakami *et al.*, J. Plasma Fusion Res. Ser. **1**, 122 (1998).

[29] T. M. Antonsen and K. R. Chu, Phys. Fluids **25**, 1295 (1982).

[30] N. J. Fisch, Rev. Mod. Physics **59**, 175 (1987).

[31] R. H. Cohen, Phys. Fluids **30**, 2442 (1987), and **31**, 421 (1988).

[32] Y. R. Lin-Liu, V. S. Chan, and R. Prater, Phys. Plasmas **10**, 4064 (2003).

[33] R. Prater *et al.*, Nucl. Fusion **48**, 035006 (2008).

[34] N. B. Marushchenko, H. Maassberg, and Y. Turkin, Nucl. Fusion **48**, 054002 (2008), and Corrigendum in **49**, 129801 (2009).

[35] N. B. Marushchenko *et al.*, Phys. Plasmas **18**, 032501 (2011).

[36] N. B. Marushchenko, C. D. Beidler, and H. Maassberg, Fusion Sci. Technol. **55**, 180 (2009).

[37] N. B. Marushchenko *et al.*, in *Proc. 14th Joint Workshop on ECE and ECRH, Santorini, Greece, 9–12 May 2006* (Heliotopos Conferences Ltd., GR-172 36 Dafni, Athens, 2006), p. 295.

[38] N. B. Marushchenko *et al.*, J. Plasma Fusion Res. Ser. **2**, S1000 (2007).

[39] V. Tribaldos and B. P. van Milligen, Nucl. Fusion **36**, 287 (1996).

[40] M. A. Tereshchenko *et al.*, in *Proc. 30th EPS Conference on Plasma Phys. St. Petersburg, 7–11 July 2003 ECA Vol. 27A, P-1.18 (2003)* (PUBLISHER, ADDRESS, 2003), Vol. 27A.

[41] F. Volpe, Ph.D. thesis, PhD thesis, IPP Garching and Greifswald, IPP Report 13/1, March 2003 (124 pages).

[42] A. P. Smirnov *et al.*, in *Proc. 13th Joint Workshop on ECE and ECRH, Nizhny Novgorod, Russia, 17 – 20 May 2004*, edited by Alexander Litvak (Institute of Applied Physics RAS, 46 Ul'yanov Str., 603950 Nyzhny Novgorod, Russia, 2005), p. 429.

[43] V. Erckmann *et al.*, Fusion Sci. Technol. **52**, 291 (2007).

[44] M. Brambilla, *Kinetic Theory of Plasma Waves. Homogeneous Plasmas* (Clarendon Press, Oxford, 1998).

[45] V. Krivenski and A. Orefice, J. Plasma Phys. **30**, 125 (1983).

[46] G. P. M. Poppe and C. M. J. Wijers, ACM Trans. on Math. Software (TOMS) **16**, 38 (1990).

[47] W. Gautschi, SIAM J. Num. Analysis **7**, 187 (1970).

[48] A. C. Hindmarsh, Serial Fortran Solvers for ODE Initial Value Problems, computation.llnl.gov/casc/odepack/odepack_home.html.

[49] M. A. Balakina, M. D. Tokman, and O. B. Smoliakova, Plasma Phys. Reports **29**, 53 (2003).

[50] S. R. de Groot, W. A. van Leewen, and C. G. van Weert, *Relativistic Kinetic Theory* (North-Holland Publishing Company, Amsterdam, 1980).

[51] N. B. Marushchenko *et al.*, Fusion Sci. Technol. **50**, 395 (2006).

[52] D. Walsh, Astrophys. Journal **159**, 733 (1970).

[53] M. Bornatici and F. Engelmann, Phys. Plasmas **1**, 189 (1994).

[54] N. J. Fisch and A. H. Boozer, Phys. Rev. Lett. **45**, 720 (1980).

[55] T. Ohkawa, Steady-state operation of tokamaks by rf heating, 1976, General Atomics Report GA-A13847.

[56] J. G. Cordey, T. Edlington, and D. F. H. Start, Plasma Physics **24**, 73 (1982).

[57] M. Taguchi, Plasma Phys. Control. Fusion **31**, 241 (1989).

[58] N. B. Marushchenko *et al.*, in *Proc. 38th EPS Conference on Plasma Physics, Strasbourg, 27 June – 01 July, 2011, P2.102* (PUBLISHER, ADDRESS, YEAR).

[59] H. Maaßberg, C. D. Beidler, and N. B. Marushchenko, Phys. Plasmas **19**, 102501 (2012).

[60] H. Maaßberg, C. D. Beidler, and Y. Turkin, Phys. Plasmas **16**, 072504 (2009).

[61] W. Kernbichler *et al.*, J. Plasma Fusion Res. Ser. **3**, S1061 (2008).

[62] W. Kernbichler *et al.*, Contrib. Plasma Phys. **50**, 761 (2010).

[63] S. P. Hirshman *et al.*, Phys. Fluids **29**, 2951 (1986).

[64] S. P. Hirshman and J. C. Whitson, Phys. Fluids **26**, 3553 (1983).

[65] J. Nürenberg and R. Zille, in *Theory of Fusion Plasmas, Proc. of the 1987 Varenna Workshop* (Editrice Compositori, Bologna, 1988), p. 3.

[66] L. L. Lao *et al.*, Nucl. Fusion **30**, 1035 (1990).

[67] W. D. D'haeseleer, W. N. G. Hitchon, J. D. Callen, and J. L. Shohet, *Flux coordinates and magnetic field structure* (Springer-Verlag, Berlin Heidelberg, 1991).

[68] Y. Turkin *et al.*, Fusion Sci. Technol. **50**, 387 (2006).

[69] Y. Gribov, *Plasma of ITER Scenario 2, Issue 4: 31 March 2005*.

[70] V. Tribaldos *et al.*, J. Plasma Fusion Res. Ser. **78**, 996 (2002).

[71] G. Grieger *et al.*, Phys. Fluids B **4**, 2081 (1992).

[72] G. Giruzzi, Nucl. Fusion **28**, 1413 (1988).

[73] J. F. M. van Gelder, E. Westerhof, F. C. Schüller, and A. J. H. Donné, Plasma Phys. Control. Fusion **40**, 1185 (1998).

[74] S. Schmuck, H.-J. Hartfuss, M. Hirsch, and T. Stange, Fusion Eng. Design **84**, 1739 (2009).

[75] N. B. Marushchenko *et al.*, in *Proc. 34th EPS Conference on Plasma Phys. Warsaw, 2 – 6 July 2007 ECA Vol.***31F***, P-5.129 (2007)* (PUBLISHER, ADDRESS, 2007).

[76] Y. Turkin *et al.*, in *Proc. 34th EPS Conference on Plasma Phys. Warsaw, 2 – 6 July 2007 ECA Vol.31F, P-1.148 (2007)* (PUBLISHER, ADDRESS, 2007).

[77] N. B. Marushchenko *et al.*, in *Proc. VII Int. Workshop "Strong Microwaves: Sources and Applications", Nizhny Novgorod, 27 July – 2 August 2008* (IAP RAS, Nizhny Novgorod, 2009), Vol. 1, p. 375.

[78] M. Thumm *et al.*, J. Plasma Fusion Res. Ser. **5**, S1006 (2010).

[79] T. Shimozuma *et al.*, J. Plasma Fusion Res. Ser. **3**, S1080 (2008).

[80] Y. Yoshimura *et al.*, J. Plasma Fusion Res. Ser. **6**, 2402073 (2011).

[81] K. Nagasaki *et al.*, Nucl. Fusion **51**, 103035 (2011).